Accepted Manuscript

Direct Fabrication of High-performance High Speed Steel Products Enhanced by LaB_6

Zhang Qiankun, Jiang Yao, Shen Weijun, Zhang Huibin, He Yuehui, Lin Nan, Liu C.T., Huang Han, Huang Xiaolin

PII: S0264-1275(16)31218-7
DOI: doi:10.1016/j.matdes.2016.09.044
Reference: JMADE 2294

To appear in:

Received date: 8 July 2016
Revised date: 12 September 2016
Accepted date: 13 September 2016

Please cite this article as: Zhang Qiankun, Jiang Yao, Shen Weijun, Zhang Huibin, He Yuehui, Lin Nan, Liu C.T., Huang Han, Huang Xiaolin, Direct Fabrication of High-performance High Speed Steel Products Enhanced by LaB_6, (2016), doi:10.1016/j.matdes.2016.09.044

Direct Fabrication of High-performance High Speed Steel Products Enhanced by LaB_6

Zhang Qiankun[1], Jiang Yao[1], Shen Weijun[1], Zhang Huibin[1], He Yuehui[1*], Lin Nan[1], Liu C.T. [2], Huang Han[3], Huang Xiaolin[1]

[1.] State Key Laboratory for Powder Metallurgy, Central South University, Changsha, Hunan, 410083, P.R. China

[2.] Center for Advanced Structural Materials, College of Science and Engineering, City University of Hong Kong, Hong Kong, P.R. China

[3.] School of Mechanical and Mining Engineering, University of Queensland, Brisbane, QLD 4072, Australia

*Correspondence to: yuehui@mail.csu.edu.cn

Abstract

A direct fabrication technology (DFT) without smelting has been developed for fabricating sophisticated high speed steel products with low pollution, near-net shaping and short process. The steel consisting of (wt. %): 6.4W, 5.0Mo, 4.2Cr, 3.1V, 8.5Co and 1.28C, was fabricated as exemplary material. The activated and reactive sintering of green compacts under vacuum with low activation energy, redox reaction enhanced diffusion and the construction of concentration gradient of alloying elements around pores, promotes the nearly full densification (>99.40%). Also, the DFT steels show high purity and superior mechanical properties. Minor strengthening agent LaB_6 (0.1 wt. %), which is easily to be accurately introduced in DFT, obviously increases the hot hardness, temper resistance, bend strength and toughness of DFT M3:2. The strengthening effect of boron atoms and La-rich complexes are proposed to directly result in the high hot hardness and temper resistance of LaB_6 containing steel.

Key word: *direct fabrication; powder metallurgy; high speed steel; rare earth; hot hardness; impurity segregation*

1. Introduction

As the basis material of human society, irons and steels also have placed heavy

burdens of energy consumption and pollution upon us [1, 2]. It's notorious that steelmaking at least generates ~7% of global anthropogenic CO_2 emissions and ~16% of the domestic total energy consumption annually [1-3]. The casting process involving sintering, coking and smelting is the prime culprit. Green manufacturing and widely applying high performance steels for reducing the total use of steel are two effective solutions [4]. Powder metallurgy (PM) is a short-process manufacturing method [5], which has been used to make around 1Mt/yr of high-performance iron-based structural components and helps reduce energy consumption by up to 30%-70% [2] in the field of near-net shaped PM automobile parts compared with traditional casting method.

As the most preferred candidates for high-quality molds, rollers, mill cutters, gear cutters, broaches, drills and screw taps [6-9], PM high speed steels (HSS) avoiding coarse microstructure also suffer with heavy pollution and energy consumption due to the complex process involving high-temperature smelting (Fig. 1). Energy-intensive and costly equipments including smelting and electroslag remelting (ESR) furnace, atomization units, large HIP and hot-work facilities [6, 10], are fundamentally necessary during the process. Near-net shaping as an essential advantage of PM is not realized either. Thus the production cost of traditional PM HSS is fatally high. Beyond that, the further development of PM HSSs, which mainly depends on optimizing the type and content of elements[11], is constitutionally restricted by the smelting process [12]. During atomization, more indispensable carbide-forming elements with high melting points, various specific gravities and different solubilities significantly increase the melting temperature, enhance the melt viscosity and bring about jamming risk [10]. As to the PM HSSs prepared using spray forming [13] or supersolidus liquid phase sintering (SLPS) [14, 15], atomization difficulty and coarse microstructure caused by liquid phase are also limiting factors.

Accordingly, a more convenient and cleaner technology via solid-state sintering and ball-mixed powders for manufacturing high-performance and near-net shaped PM HSS products was proposed, named as direct fabrication technology (DFT). Low density (85%-95%) [5] and high impurity content (O[16], S and P [17]) are the common shortages of sintered PM steel parts. Further, impurity contents directly determine the grade classification of PM HSSs. Can DFT steel pass the thresholds of density and impurity? Minor LaB_6 was particularly introduced into DFT steels, preliminarily aiming at strengthening grain boundaries (GBs) by boron segregation [21-25] and simultaneously purifying the steel via the absorbing effect of rare earth (RE) complexes [18, 19]. During smelting, the accurate and lossless additions of high melting elements and the elements sensitive to oxidation, such as boron [20-23] and RE [18, 19], are always tough puzzles. Here, activated sintering was adopted for deoxygenating and enhancing the densification. The densification behavior, strengthening mechanism of LaB_6 and mechanical properties of DFT steels, as well as the feasibility of near-net shaping, will be mainly investigated.

Fig. 1. The graphical comparison of DFT and gas-atomization & HIP process.

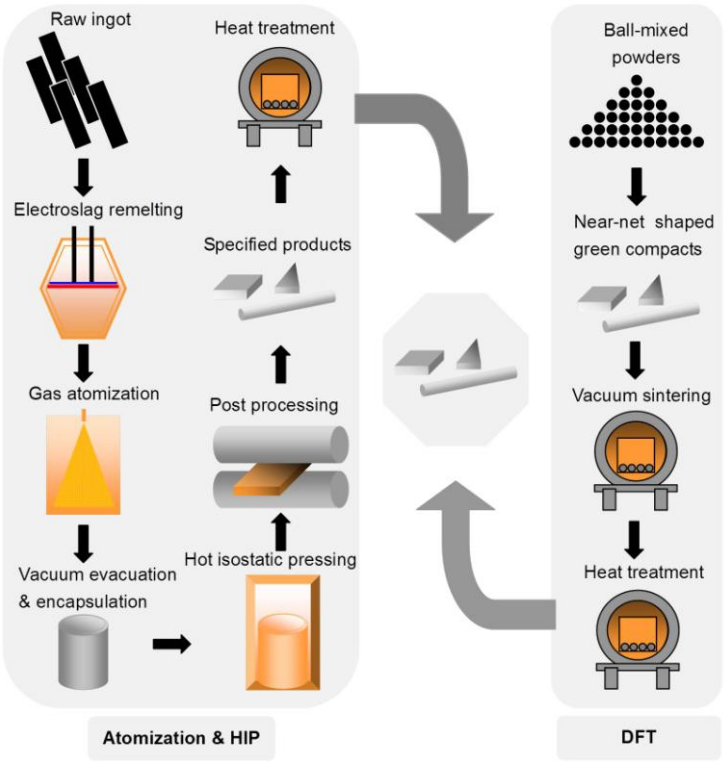

2. Experimental method

AISI M3:2 high speed steels (ASP30, SKH40) consisting of (wt. %): 6.4W, 5.0Mo, 4.2Cr, 3.1V, 8.5Co, 1.28C and Fe, were fabricated as exemplary materials via the direct fabrication technology (DFT). The technological process of DFT is graphically presented in Fig.1, in comparison with traditional gas-atomization & HIP process. The fine carbonyl iron powders (Fe, 2-4μm) prepared by purifying the hydrogen-reduced direct reduction iron (DRI) via carbonylation and decarbonylation in a closed circulation system, in which CO is recurrently used [24], were applied. The production of DRI avoiding smelting-reduction consumes less energy and produces less hazardous gas emissions[24]. Commercial carbide powders (WC, Mo_2C, Cr_3C_2 and VC) and elemental powders, the producing of which is mainly related to the cleaner hydrometallurgy process, are applied for in-situ forming hard carbides. Raw powders were mixed in alcohol in a planetary ball mill for 72h with a ball-to-powder weight ratio of 5:1. Mixtures were then successively granulated, dried, preoxidized and cold pressed at 150 MPa to designed shapes. After sintered at 1150℃-1190℃ under vacuum (10^{-3} Pa) based on designed sintering schedules, specimens were preheated and austenitized at 1165℃ in salt for 10 min, quenched in oil and triple tempered at 560℃ for 1h. The impurity content (Table 1) of admixed powders and as-sintered steels were measured using inductively coupled plasma emission spectrometer (ICP, IRISAdvantage1000), LECO CS-444 C/S analyzer and LECO TC-436 N/O analyzer. The DTF M3:2 steels added with 0.05, 0.1, 0.15 and 0.2 (wt. %) LaB_6 were named as 05LB, 10LB, 15LB and 20LB.

Rockwell Hardness was measured with a load of 150 kg. Bend strength was tested with a span of 14.5 mm and a sample dimension of 5×5×25 mm. Fracture toughness was measured according to single edge notched beam (SENB) method [25]. Tensile fatigue life was recorded until failure with a stress ratio of 0.05 and a frequency of 1Hz. The applied

tensile stress was determined by $\sigma_M=0.65\sigma_b$. Here, the values of tensile strength of annealed M3:2 and 10LB are 971~995 MPa. The tensile stress of ~650 MPa is accordingly applied. The shape and dimension of the sample for tensile fatigue test is shown in Fig. S1. And the red hardness was tested after soaked at 560℃, 600℃ and 650℃ for 4 hours and air cooled to room temperature[18]. In-situ hot hardness was measured at 600℃, 700℃ and 800℃ using a hot hardness tester under Ar gas with a soaking time of 15min.

Table 1 Chemical compositions (wt. %).

	C	O	S	N	P	LaB_6	B
Commercial	1.28	⩽0.015	⩽0.030	⩽0.030	⩽0.030	—	—
M3:2 Mixes	2.12	2.2000	0.0580	0.0120	0.0090	0	—
DFT M3:2	1.26	0.0022	0.085	0.0091	0.0050	0	—
DFT 10LB	1.24	0.0175	0.089	0.0082	0.0050	0.10	0.0310

Scanning electron microscopy (SEM, FEI Nano230) was used for microstructure analysis. Image J software was used for image quantitative analysis. Field emission electron probe micro-analyzer (FE-EPMA, JEOL JXA-8530F) was applied for element analysis. Secondary ion mass spectroscopy (CAMECA NanoSIMS 50) with a Cs primary source (16 keV) was used for precisely measuring boron and other light elements. A scan area of 25×25 μm^2 and an acquisition time of 45 min were applied. X-ray diffraction (D/MAX-255, Cu Kα) and transmission electron microscopy (TEM, JEM 2100F, 200kV) were also employed. Thin film samples for TEM were prepared by ion milling.

3. Results and discussion

Compared with the PM HSSs prepared from pre-alloyed powders using HIP [9], SLPS [7, 8, 26] or other densifying method [14, 15, 27, 28], several crucial issues must be urgently considered and clarified upon DFT steels: 1) the densification behavior via solid state sintering (SSS), 2) the control of carbon, alloying elements and impurity elements (O,

S, P and N), 3) composition homogenization and microstructure, 4) the realization of near-net shaping, 5) mechanical properties and 6) carbon emissions. Accordingly, the experiment was carried out in sequence.

3.1. Densification behavior of DFT M3:2 steel

3.1.1 Carbon-oxygen redox reaction induced activated sintering

XRD patterns, evolutions of carbon content and relative densities of DFT M3:2 after sintered at given sintering temperatures (ST), and DSC curves are shown in Fig. 2(a-c). After milled for 72h, elongated Fe particles and crushed carbides with an average size of about 0.53 μm were obtained as shown in Fig. 2 (d), since the size of mixed powders didn't visibly change below 800℃. The non-equilibrium stress on particles from all directions during ball-mixing not only results in refined grains but also greatly enhances the distortion energy [29], in favor of strengthening sintering.

After milling, designed preoxidation and drying of admixed powders were synchronously achieved in a drying oven with low oxygen partial pressure. Elemental powders (Fe and Co), other than chemically stable carbides, suffer high sensitivity to oxidation [30-34]. Regarding that the oxygen dissociation pressure (P_{O2}) of CO is lower than those of the oxides of Fe and Co [35] above 600℃, which are the main oxygen donors, the redox reactions between carbon and oxides can thermodynamically occur. Actually, the evolved gas generated from the reduction of oxides by active carbon in the compacts sintered above ~760℃ under vacuum has been approved to mainly encompass carbon monoxide [36] based on an overall reaction [35]:$C + MeO \rightarrow Me + CO$. *Me* represents metal. Thus, the carbon content was controllably designed based on the oxygen content of preoxidized powders. Based on the carbon content during sintering, the contents of chemically fixed oxygen (MeO) and absorbed oxygen are 1.07-1.18 wt.% and 1.02-1.13 wt.%. The latter can be adequately drained out under vacuum. Consequently, the intensity

values of direct CO/CO_2 emissions here are about 18.7-20.6 kg/t, compared with the values of 1.38-2.8 t CO_2/t [2] during traditional steelmaking process.

Fig.2. *The (a) XRD patterns, (b) carbon and density variations and (d-h) SEM (back-scatter electron, BSE) images of M3:2 steels after sintered at different temperatures. (c) displays the DSC curves of as-sintered DFT M3:2 and 10LB. (h) is etched morphology. (i) shows the partial diffusion at 1000 ℃. (j) and (k) are the construction and model of alloying elements segregated around closed pores.*

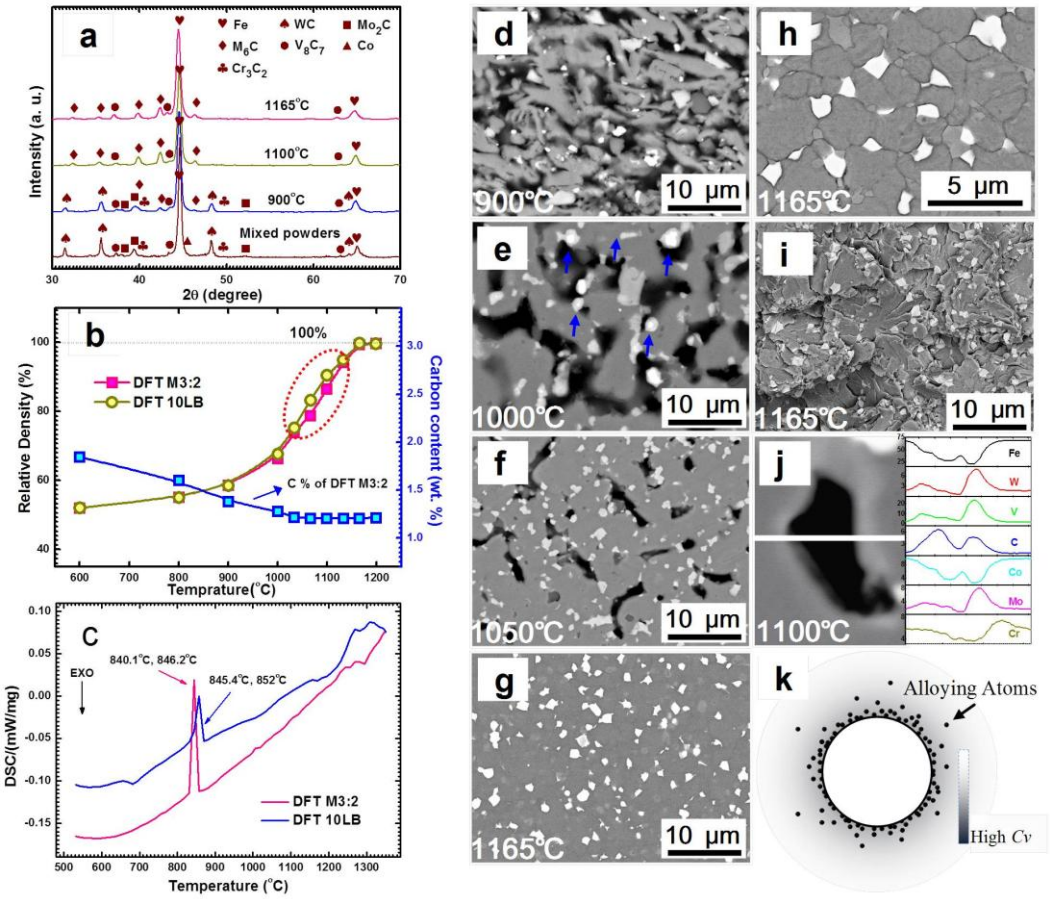

The theoretical density (TD) of annealed AISI M3:2 is ~8.04 g/cm^3 and the density of the green compact of DFT M3:2 was specially set as ~50% TD (4.05-4.08 g/cm^3) for facilitating gas-emission. According to Fig. 2(b), the carbon-oxygen reaction mainly occurred before 1025℃ since the carbon content exhibits slight variations (1.2-1.25 wt.%) at higher temperatures. Fortunately, the compact density at 1025℃ is less than 73.95%, which means open pore channels let the CO gas adequately escape under vacuum. Therefore, it's of importance to design a sintering platform no higher than 1025℃ to

ensure sufficient redox reaction and avoid gas sealing before pore closure. Vigorous carbon-oxygen reactions facilitate the formation of highly active reduced powders [35] and lay a foundation for complete densification and material purification.

3.1.2 Coarsening and densification

Actually, diffusion is the most important sintering mechanism and based on modern defect theory, atom diffusion is mainly driven by the difference of chemical potential (CP) and vacancy concentration (VC) [31, 34]. During the initial stage (600℃-900℃), the elongated and distorted Fe particles slightly recrystallized (Fig.2 (d)). Based on the pressing-induced contact among particles and Van der Wals forces (VDM), the amplitude of atomic vibration increases with temperatures [37, 38] and then bonding interface formed (800℃-900℃), namely sintering necks (inset in Fig.2 (d)).

At intermediate stage (900℃-1100℃), the massive nucleating and coarsening of γ-Fe grains accelerate the transformation from interfaces of iron particles to grain boundaries (GBs), regarding the larger energy of the former. Interestingly, the sample at 1000℃ shows larger average pore size than that at 800℃ and 900℃. Akash [32] also observed pore growth during initial and intermediate stage. Here, the growth is ascribed to neck growth, asymmetrical grain size, particle coalescence [33] and differential sintering [32]. Neck growth can be explained by the classical two sphere model [37, 38]: $\Delta\sigma = \gamma\left(\frac{1}{R_1}+\frac{1}{R_2}\right)$ (1) and $\Delta\mu = \sigma V_m$ (2), where σ is Laplace tensile stresses along interface, γ is surface tension, V_m is mole volume, μ is chemical potential, R_1 and R_2 are the principle radius of curvature. That is, the neck with lower R shows larger σ and higher $\Delta\mu$ of vacancy. Then excess vacancies consistently exist during densification[34]. The atom migration towards the neck region with lower R behaves as neck growth.

During the intermediate stage, the homogenizing diffusion spontaneously lowering the composition fluctuations among carbides and matrix [29], leads to particle growth and

forming carbide complexes, as a result of reactive sintering [39]. The average carbide size gradually increased from 0.53 μm (900℃) to 1.15 μm (1165℃). The gradient diffusion of elements Fe, Mo, Co and Cr are responsible for the annular carbides (Fig. 2 (e) and (i)) with white WC as the core at 1000℃. The XRD results indicate that complex carbides (MC and M_6C) started to form at 1000℃ or even 900℃. The annular carbides (M_6C) disappeared after 1025℃ (Fig. 3 (a)). With the coarsening of γ-Fe grains, carbides were pushed towards interfaces and the complex carbides generated on the basis of randomly gathered carbides. For instance, gathered WC and Mo_2C carbides tend to form M_6C and VC tends to form MC, with the participation of Fe, C and Cr [8].

Fig.3. SEM images (BSE mode) of DFT M3:2 at (a) 1025 ℃, (b) 1075 ℃ and simplified models of (c) the formation and (d) the role of secondary necks. The big and small spheroids in (c) indicate γ-Fe and various carbides, respectively. In (d), dashed lines are matrix, blue circles are carbides, orange circles are pores and orange lines are grain boundaries (GBs).

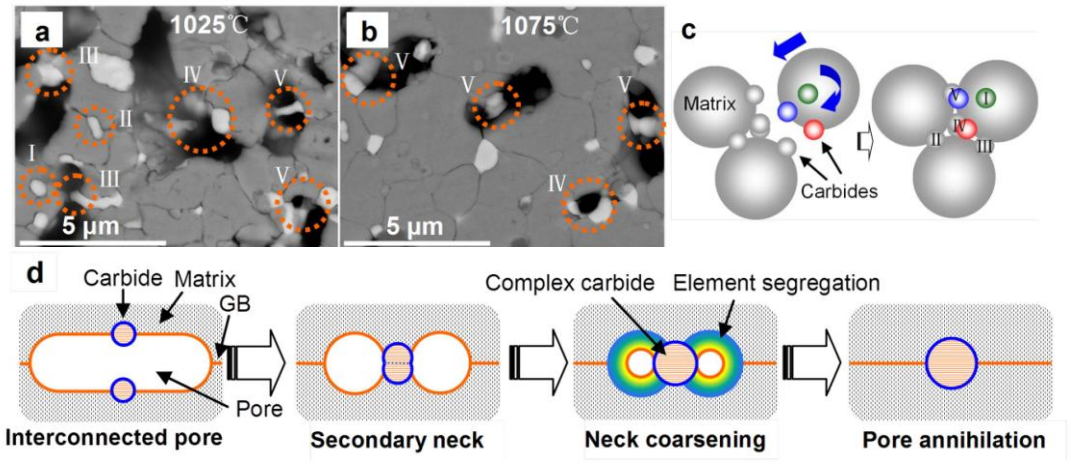

During intermediate stage, numerous carbides locate on particle surface or necks (Fig. 3(a)). Based on marks, five kinds of carbides were proposed as modeled in Fig.3 (c): Ⅰ) the carbides inside grains; Ⅱ) the carbides entrapped in GBs by adjacent Fe grains via original mechanical pressing or recrystallization; Ⅲ) the carbides forming carbide/matrix

necks benefiting from shortened interparticle distance of Fe grains; Ⅳ) the carbides forming carbide/carbide necks along GB via particle re-arrangement or bulk shrinkage; Ⅴ) the carbides forming carbide/carbide necks at triple GB junctions. Here, the necks of Ⅲ, Ⅳ and Ⅴ are proposed to be named as "secondary necks" (SN). During the formation of SN, obviously, complex carbides (M_6C and MC) gradually formed with the involvement of Fe. As proved above, pore serves as vacancy source and the margins with small R are rich in vacancies [38] and atoms deviating from equilibrium position with higher kinetic energy. The segmenting effect of SN remarkably reduces the R value considering the constant pore volume at certain ST [34], accelerating diffusion and the formation of closed pores.

In Coble's model [40] of final stage of sintering, grain boundary as atom source is not counted in. But Kang's model [41] predicts that grain boundary diffusion governs the densification in the case of inconsiderable grain growth and lattice diffusion dominates when grain growth distinctly occurs. In DFT HSSs with dispersed micro carbides, grain growth is partially suppressed by remained carbides (Fig. 2(h)). To be simplified, both mechanisms are considered responsible here.

Interestingly, after sintered according to designed schedules, the isolated pores in final stage show a gradient enrichment of alloying elements along pore margin, which is gradually whiter than matrix in BSE mode images (Fig. 2(j) and (k)). The segregation may be contributed by the surface diffusion & evaporation from carbides. Or, at high temperature, the alloying atoms from the sharp corner of carbides substitutionally solutioning into matrix cause larger lattice distortion energy or elastic strain energy which is related to the radius of atoms [40]. Then they diffuse towards bigger carbides, pores or GBs for reducing the interface energy and then the lattice distortion energy, similar to Ostwald ripening [37]. Meanwhile, the faster C atoms also show segregation. Then the concentration gradient of alloying elements and vacancies thermodynamically enhance the

diffusion of Fe towards vacancy sources via lattice diffusion or GB diffusion to neutralize the gradient of alloying elements. Further, with the participation of Fe, the segregation of C around pores constitutionally enhances the diffusion of carbide-forming elements[42] which show high affinity with C, behaving as lowered fusion point (higher than sintering temperature). Vacancies migrate towards an opposite direction and pore shrinkage persistently occurs. The segregation could not be observed in intermediate stage. It may be due to the slower diffusion rate and lower solubility of alloying elements in austenite at lower temperature [42].

Accordingly, it's reasonable to hypothesize that SN and element segregation modify the densification during mediate and final stage as modeled in Fig. 3(d). The shape evolution of carbides and the role of GB are not taken into account. As to the sintering of chemically unstable polycrystalline solid, the diffusion-induced grain-boundary migration (DIGM) sometimes causes pore/GB separation [34], contributing to forming intra-granular pores, which can be mostly avoided in DFT steel via the pining and strengthening effect of carbides and SNs. Almost no intra-granular pore linked to carbides can be observed during intermediate stage and all pores attach to GBs (Fig. 3(a) and (b)). The draining out of remaining vacancies via grain boundary diffusion and lattice diffusion is considered the last step for final densification. Then near full densification (>99.4%) of DFT M3:2 is obtained after sintered at 1165℃. Final temperatures of 1165℃ and 1150℃ are chosen for M3:2 and 10LB, respectively.

3.1.3 Apparent activation energy

Classic Arrhenius equation is applied for evaluating apparent activation energy in main SSS process (from 1000℃ to 1132℃ where main shrinkage occurs) by linearly plotting the $(\ln K - \frac{1}{T})$ curves [37]: $\ln K = \ln A - \frac{Q}{RT}$ (3), where K is the sintering rate constant calculated from ΔL, T is sintering temperature, Q denotes apparent activation

energy, *R* and *A* are constants. The *Q* values of DFT M3:2 and 10LB are 109.56 kJ/mol and 108.09 kJ/mol, which are less than the common 183-233 kJ/mol of sintered M3:2 HSS [38] prepared by sintering pre-alloyed atomized powders. Ball-milling induced distortion and surface energy only strengthen the sintering, but show negligible effect on the intrinsic activation energy [14]. In general, reactive sintering shows lower Q than common sintering [30, 34]. Hence, the low energy values of DFT steels are considered to be mainly contributed by the activated sintering via carbon-oxygen reaction and reactive diffusion[39].

Fig.4. (a) Oxygen content of as-sintered steels, (b)near-net shaped lathe tools and SEM (BSE mode) graphs of microstructure of as-tempered (c) DFT M3:2, (d)10LB, (e)20LB and (f) fracture morphology of as-annealed DFT M3:2 steel.

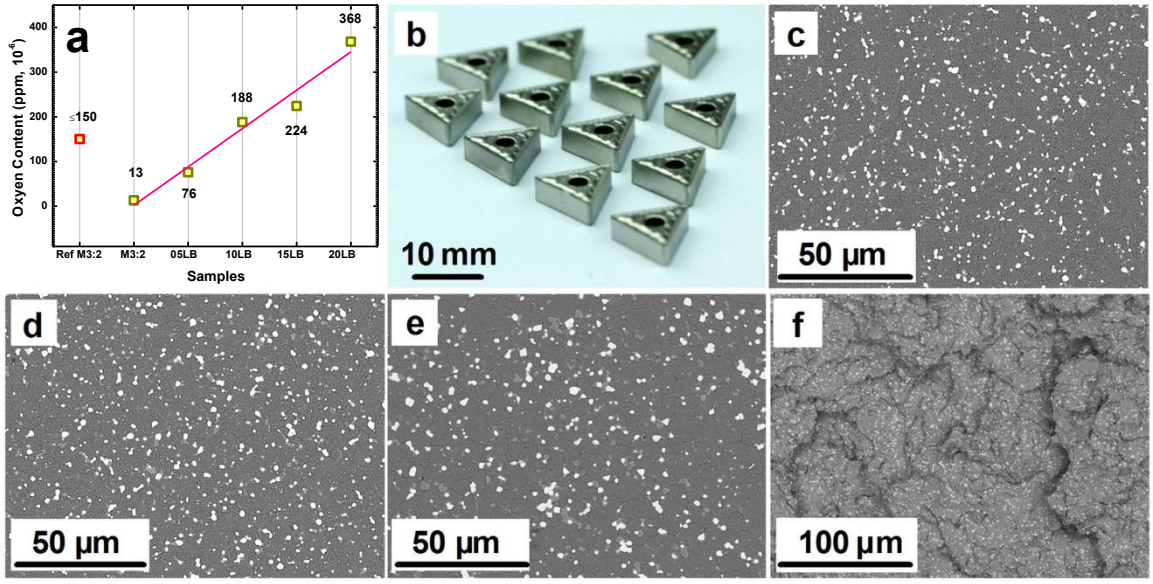

3.2. Composition, microstructure and phase analysis

Obviously, the content of W, Mo, Cr, V and Co can be precisely controlled by accurately adding stoichiometric carbides and elemental powders during DFT. The carbon content has been solidly handled via designed reaction between carbon and exogenous oxygen controlled by preoxidation (Table 1). The contents of N, P and S depend on raw purified powders and are less than 100ppm in DFT M3:2. The sulfur (0.058 wt. %) in

mixed powders noised by binders can be exhausted by thermal degreasing. Amazingly, the oxygen content in DFT M3:2 (13ppm) is far less than the standard value (150ppm) unlike common PM parts. However, the oxygen content increases with LaB_6 content (Fig. 4 (a)).

Fig. 5. EPMA mapping results of as-tempered 10LB steel. The values on the top right corner of each figure indicate the top concentration (red).

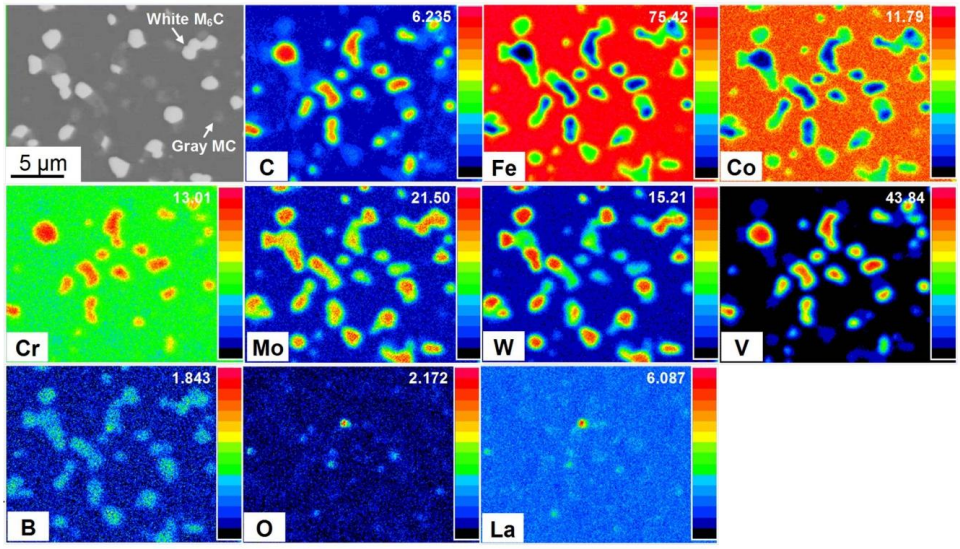

DFT 10LB was chosen to directly manufacture lathe tools with complex three-dimensional shapes (Fig. 4(b)). The precise preparation of rake faces, flanks and chip breaker grooves of near-net shaped lathe tools was achieved. The total dimensional tolerances were controlled within ±0.05mm considering the oxidation and decarburization during sintering and heat treatment. As shown in Fig. 4(c-e), the densification below liquidus radically avoids forming coarse carbides or eutectic ledeburites, which are inevitable during SLPS [9, 14]. From the low-magnification fracture image in Fig. 4(f), we reconfirm the extent of densification of sintered bulks. The sintering window (SW) of DFT M3:2 is ~30K and the SW of 10LB is narrowed to 15-20K, both of which can be easily controlled.

MC and M_6C are the main carbides in as-sintered, as-quenched and as-tempered M3:2 based steels [8], the total carbide volumes in which are 19±1.5%, 9±1% and 16.5±1.5%, respectively. Minor LaB_6 additions exhibit little effect on the types and total

volumes of carbides. 10LB shows bigger particle size of carbides (1.3μm) and grain size of tempered martensite (5.4μm) than M3:2 (1.15μm and 4.1μm). More LaB_6 additions lead to further coarsening of both matrix and carbides. The fracture morphology of as-sintered M3:2 steel exhibits transgranular fracture with tearing edges and symmetrical quasi-cleavage. It should be noted that no additional thermal deformation was implemented here. It somehow proves the metallurgical bonding of raw powders after solid state sintering.

Based on Fig. 5, almost all elements uniformly distribute in α-Fe. The white M_6C carbides belonging to $(A_3B_3)C$ or $(A_4B_2)C$ [14, 34] contain about 45.5 Fe, 16.5Mo, 20.8W and 6.1Co (at. %), with uniform distributions. In the grey MC carbides mainly composed of 46.3V, 13.8Mo, 12.7W and 6.6Cr (at. %), the gradient distribution of elements in MC is corresponding to the results [17, 26] in the HSSs made from pre-alloyed powders. Godec [26] proved that the chemical inhomogeneity in MC can't lead to the heterogeneous crystallographic orientation of carbides based on EBSD analysis.

3.3.Mechanical properties of as-tempered DFT steels

Almost all mechanical properties of DFT 10LB in Fig. 6(a) show fair comparability with commercial Ref M3:2 high speed steel. As to intra-group comparison, minor LaB_6 further improves both bend strength and fracture toughness of M3:2 steel. 10LB shows peak values of bend strength and fracture toughness. However, the hardness varies little with LaB_6 content. As proved above, the oxygen content increases with LaB_6 additions. High oxygen content in steels generally leads to decreased fatigue life [26]. Surprisingly, DFT 10LB shows better fatigue performance (1.35×10^5 cycles) than DFT M3:2 (0.26×10^5 cycles).

Minor LaB_6 additions also modified the temper resistance of DFT M3:2 after triple tempered at 540℃-650℃ (Fig. 6 (b)). The red hardness values of all steels slightly

decrease by 0.5-1 HRC after soaked at 560℃ for 4h and remarkably decrease above 600℃ (Fig. 6 (c)). However, red hardness increases with LaB_6 content and 20LB shows the highest values at both 600℃ and 650℃. Shimada [22] proves that boron increases the temper resistance of stainless steel via postponing martensite decomposition and the transformation of retained austenite.

Fig. 6. (a) Room-temperature mechanical properties, (b) temper resistance, (c) red harness and (d) in-situ hot hardness (tested at 600℃, 700℃, 800℃ after soaked for 15min) of as-tempered HSSs.

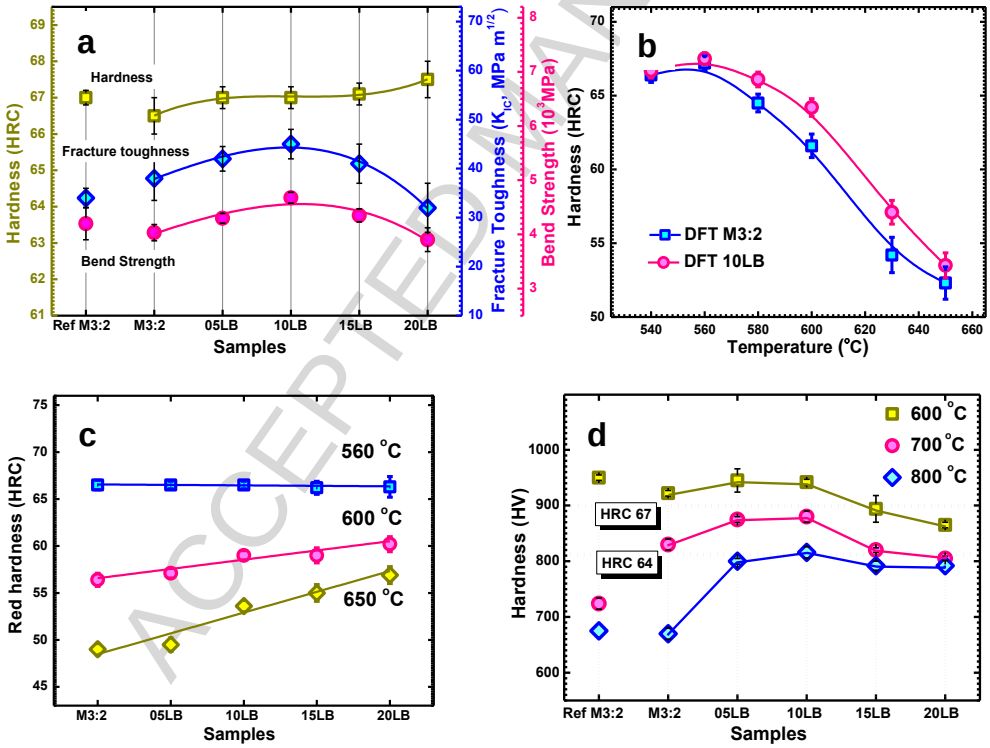

The in-situ hot hardness results (Fig. 6 (d)) show that almost all samples maintain above 900 HV at 600℃. It indicates the inherent resistance of PM HSSs to instantaneous overheating. But the hardness values of Ref M3:2 decrease remarkably at 700℃ and 800℃ to 724±10 HV and 675 HV, respectively. DFT 10LB shows the highest values at both 700℃ (880±10 HV) and specially, 800℃ (816±10 HV). Differing from the red hardness increasing with LaB_6 content, more LaB_6 additions (>0.1 wt. %) lead to the slight decrease

of hot hardness. In Pan's work, the hot hardness of $W_9Mo_3Cr_4V$ tool steel at 600℃ is about 600-650 HV [8]. The much less hardness decrease at 600℃ here may be related to the shorter soaking duration. Ferrous HSS has been widely applied below 600℃, restrained by its inherent phase transitions (segregation, precipitation and recovery) at higher temperatures. Rong [9] demonstrated that experiencing at 700℃ for 1h, the plate martensite in as-tempered HSS had fully recovered and equiaxed grained ferrites had formed along with the precipitation and coarsening of secondary carbides, which are proved to be not controlled by carbon diffusion but by the volume diffusion of alloying elements [7]. Obviously, LaB_6 delays the hardness decrease of DFT HSSs via a latent mechanism.

3.4. The role of La and B

First, the high yields of La (>99.2%) and B (>95%) in 10LB steel verify that negligible melting loss of La or B occurred during DFT. It means the accurate addition of the La and B sensitive to oxidation during smelting [9] can be easily achieved using DFT. Further, chemical states and distributions of La and B in DFT HSSs should be made clear.

Regarding the low sensitivity of EPMA for boron and the noise of molybdenum peaks [7], Fig. 5 imprecisely exhibit the boron distribution and Nano SIMS was applied for cooperatively analyzing trace and light elements. The contents (ppm) of O, S, N, P and B in 10LB are 175, 89, 82, 50 and 310 (Table 1). Similar to Fig. 5, the ion map of $^{12}C^-$ accurately identifies the distribution of C in the orange MC, green M_6C and blue Fe. By contrast, $^{11}B^-$, $^{16}O^-$ and $^{32}S^-$ show almost overlapped distributions as nano dots. $^{11}B^{14}N^-$ also exhibits fuzzy overlaps with boron, while $^{31}P^-$ shows almost no segregation.

Combined with Fig. 5 that O overlaps with La, it can be speculated that element La also overlaps with B, S [19] and N. The rest of La atoms show uniform distribution in matrix with a negligible abundance due to the low solubility of La in austenite [18, 19].

Further TEM/EDS analysis (Fig. 8) proves that La-rich particles mainly exist as core-shell dots along carbide/matrix boundaries or inside the Fe grains. The HRTEM image of the core-shell boundary indicates that the core (Ⅱ) is LaB_6 and the shell (Ⅰ) is amorphous, which mainly contains O, La, Al, S, Fe, Ca and Si. The total contents of Al, Ca and Si in DFT 10LB are 0.028, 0.001 and 0.23 (wt. %, ICP), respectively. These impurities in shell may derive from the raw powders. The contents of O and Fe in core may be interfered by covered shell. Boron is not included in calculation but shows obvious peaks in both EDS curves. In sum, the core mainly contains LaB_6 and the shell consists of O, Al, S, Ca and Si, differing from the La-O or La-O-S complex formed via oxidation in La-containing cast steels [19]. However, the existence of La, B and Fe in shell can't be denied.

Fig.7. Nano SIMS ion maps of ^{11}B, ^{12}C, $^{11}B^{14}N$, ^{16}O, ^{32}S and ^{31}P in as-tempered DFT 10LB steel.

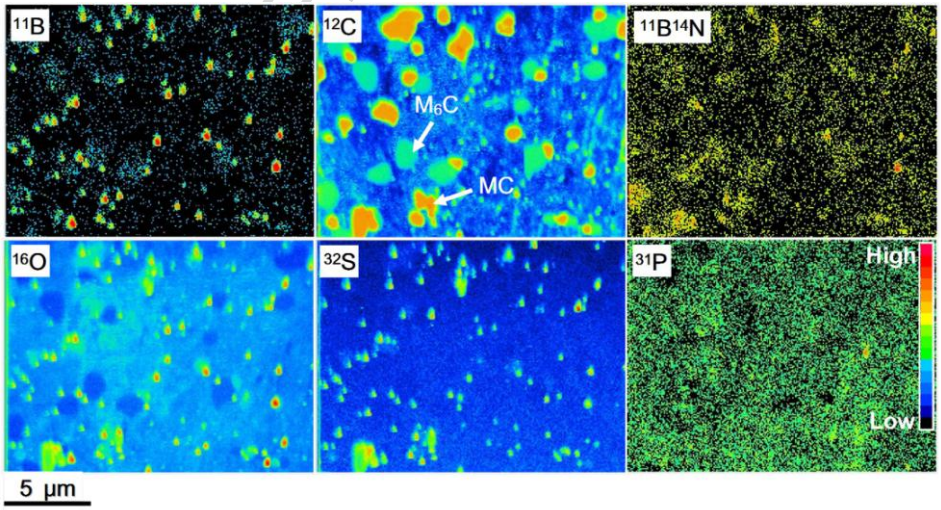

Accordingly, the high oxygen content in DFT 10LB can be explained by the purifying effect of LaB_6-rich complexes at the cost of immobilizing oxygen in shell. In one hand, the pining of oxygen reduces the possibility of forming trapped gas in closed pores and helps final densification. Besides, dispersed LaB_6-rich dots may be helpful for retarding the dislocation motion and recovery in service, similar to the effect of oxides in oxide dispersion strengthened (ODS) steels [43]. Fortunately, the dispersed dots didn't worsen

the fatigue properties of 10LB steel as proved.

Obviously, some LaB_6 additives exist for relieving the impurity hazard and some decompose into B and La atoms diffusing into carbides or ferrous matrix. Boron atoms show a distribution in M_6C carbides (green) with the second priority and almost uniformly lie in matrix with the least content (Fig.7). It means the non-equilibrium segregation of boron along vacancy sinks (i.e. grain boundaries), which commonly occurs in boron containing steels during cooling [18, 21, 44], are not detected in the as-tempered DFT 10LB. Similarly, Keown [45] also stated that no boron segregation occurs in Cr-Mo-V creep-resisting steel after tempered at 700℃, though Karlsson [18] demonstrated that boron atoms are very mobile and segregate even after cooled from below 500℃. In the steel with massive second phases and molybdenum atoms which show high affinity with boron [22, 23, 45], the boron acting as mobile vacancy-solute atom pair, diffuses towards Mo-rich area (M_6C) and vacancy sinks such as high-angle boundaries, dislocations and other defects with high mismatch degree [22]. Then the total interface or distortion energy is reduced [45]. It has been proved that the participation of Mo remarkably affects the boron distribution [45], which may be related to the segregation of B in M_6C.

Fig. 8. (a, e) TEM images of La-rich dots and the corresponding (b) high resolution TEM (HRTEM) images, (c) Fourier pattern and (d) EDS results.

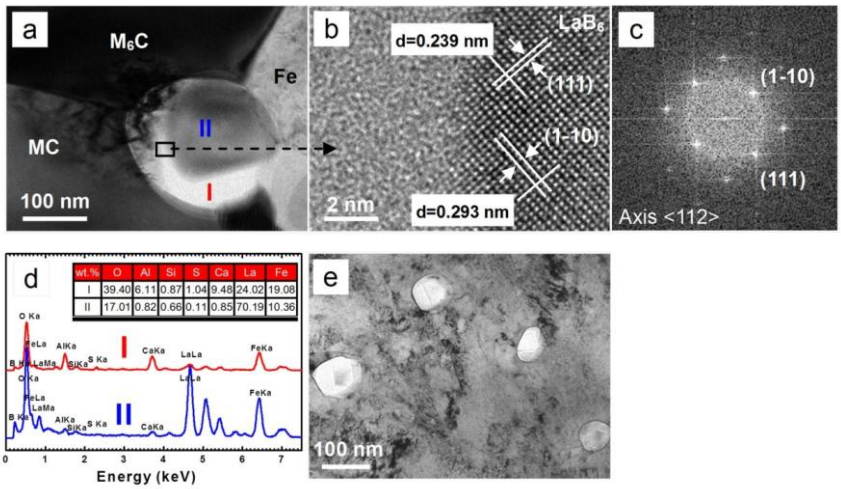

The role of B is complicated in the DFT steels with multi-elements. First, LaB_6

increased the density of M3:2 of 99.40% to higher than 99.75% and lowered the sintering temperature. Commonly, the active boron atoms dissolved into matrix are able to stabilize undercooled austenite [46] and improve the hardenability of steel [21, 22, 44], which offers boron a great potential in substituting costly alloying elements in steel. Furthermore, the segregation of boron in M_6C means forming $M_6(C,B)$ while the lattice parameter increases from 11.287 Å to 11.381 Å (a_{Fe3W3C}=11.1094 Å, PDF#41-1351). Based on the nano-indentation results, micro harnesses of the M_6C in DFT M3:2 and the $M_6(C, B)$ in 10LB are 2992±120HV and 3090±170 HV, respectively. The values are higher than the 2000-2500HV of M_6C in tool steel as reported by Casellas [47]. It may be related to the different composition and smaller carbide size in DFT steel. The enhanced abrasive resistance and hardness contributed by boron have been reported [22]. The harder boro-carbides may partially contribute to the red hardness increasing with LaB_6 content. However, the slight decrease of hot hardness occurred when the LaB_6 additions are more than 0.1 wt.%. Here, two possible reasons are proposed. First, more LaB_6 additions lead to distinctly coarser carbides and tempered martensites (Fig.4), inherited from the coarsened austenites. In other words, with more LaB_6, we obtain less grain boundaries and smaller amount of carbides, which play significant roles in inhibiting the recovery and recrystalization of martensites [9]. Second, the oxygen content linearly increases with LaB_6 additions. It means the oxygen that could has been exhausted by redox reaction and vacuum, is instead fixed by LaB_6. Similarly, the content impurities including Ca, Mg, Si and Al, which can be partially drained out by vacuum[14], may also increase with LaB_6 by forming the amorphous “shell” with oxygen around the “core”. This research can not deny the existence of La and B in shell. The condition containing more oxygen chemically increases the risks of the oxidation of La or B. Considering the softening temperature of the amorphous layers, more layers or possibly thicker layers may become unstable at high

temperature [20] and then affect the high-temperature performance of steels.

10LB steel shows smaller lattice parameter (2.957 Å) of 560℃-tempered matrix than DFT M3:2 (2.980 Å), while the value of $a_{\alpha\text{-Fe}}$ is 2.8664 Å (PDF#06-0696). It may be related to the substitutional solution of B and interstitial solution of C in α-Fe[23]. Also, 0.1 wt.% LaB_6 increases the initial α-γ transition point of M3:2 from 840.1℃ to 845.4℃. It indicates that the nucleation of γ-Fe is postponed, which may be related to the defects strengthened by boron[23]. The recovery and growth of tempered martensite may be restrained via similar effects. The dispersed and fine LaB_6 complexes as stabilized particles also show potentials in pinning dislocations and grain boundaries during over tempering[19].

Fig. 9. TEM images of steel DFT M3:2 (a) and 10LB (b, c) after heated at 800 ℃ for 15min and water quenched, the HRTEM images and Fourier patterns of the rod-like (d, e) and needle-like (f, g) carbides in 10LB were displayed. (d) and (f) were selected from (c) as marked.

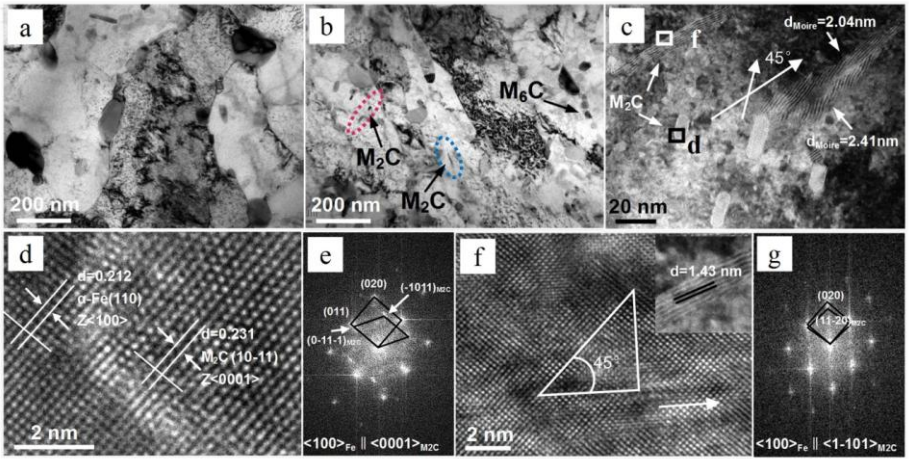

DFT M3:2 and 10LB after heated at 800℃ for 15min and water quenched were characterized by TEM. Obviously, plate martensite recrystallizes with the formation of massive equiaxed grains in both of the two steels, and M3:2 shows more coarsened ferrite grains and precipitated carbides. In 10LB, the original martensite still remains faintly lamellar structures with dispersed fine carbides. As marked in Fig.9 (b) and (c), in addition

to the primary MC and M_6C carbides, fine rod-like and needle-like secondary carbides inside the recrystallized grains and dot-like carbides along martensite plates in 10LB can be observed. The dot-like carbides are W and Mo-riched M_6C, in agreement with reported results of over-tempered steels [7]. The other two kinds of carbides show similar composition (M_2C) but different morphology. Further HRTEM analysis of the two carbides in Fig. 9(d) and (f) exhibits that the rod-like carbides with a size of 11μm×17-35μm are hexagonal M_2C showing $(10\text{-}11)_{M2C}$// $(110)_{Fe}$ and $[0001]_{M2C}$//$[001]_{Fe}$. The needle-like carbides (10-18μm×~100μm) are also M_2C with a relationship of $(11\text{-}20)_{M2C}$//$(020)_{Fe}$ and $[1\text{-}101]_{M2C}$//$[001]_{Fe}$, which corresponds to the Pitsch-Schrader relationship [7]. The latter M_2C shows various Moire fringes with different spacing and orientations. It implies that two kinds of M_2C coexist inside the reheated matrix and the angle between $M_2C(10\text{-}11)$ and the other $M_2C(11\text{-}20)$ is 45°, as plotted in Fig. 9(c) and (f). The precipitation of M_2C and M_6C agrees with the transformation sequence of $M_3C \rightarrow M_2C/M_{23}C_6 \rightarrow M_6C$ in 700℃-tempered tungsten steels[8]. It should be mentioned that the spacing of α-Fe (110) in DFT M3:2 (d=2.05 Å) is statistically smaller than that in 10LB (d=2.12 Å) after heated at 800℃, while $d_{(110)}$=2.0268 Å according to PDF#06-0696. Considering that the substitutional solutioning of B in α-Fe [18] decreases the value of $d_{(110)}$, the increased inter-planar spacing may be related to the effect of boron on postponing the precipitation and growth of secondary carbides [7], as shown in Fig. 9(a) and (b). In other words, B may delay the precipitation of dissolved atoms from oversaturated tempered martensite or the La-B-O complexes impede the recovery of martensite. The higher γ-α point of 10LB in Fig. 2(c) than that of DFT M3:2 also proves this point. In sum, the strengthening effect of boron atoms and La-B-O complexes are proposed to directly result in the high hot hardness and temper resistance of LaB_6 containing steel.

4. Conclusions

A convenient DFT method for directly manufacturing high-performance powder metallurgy high speed steel was proposed in this work. Lower cost, shorter process flow, less carbon emission and near-net shaping can be realized via DFT in comparison with traditional atomization & HIP process. The near full densification (**>** 99.4%) of DFT M3:2 was attributed to the enhanced activated sintering via carbon-oxygen redox reaction and the reactive sintering involving constructing element segregation around pores and secondary necks. Minor strengthening agent LaB_6, which is easily to be accurately introduced in DFT, obviously increased the hot hardness, bend strength and toughness of DFT M3:2. The steel M3:2 added with 0.1 wt. % LaB_6 exhibited the highest hardness of 816 HV at 800℃. A core-shell structure with LaB_6 serving as the core and gathered impurities (O, Al, Ca, Si, etc.) as the shell, evidently proved the purifying effect of LaB_6. The Nano SIMS further indicated that trace S gathered around LaB_6 but P distributed uniformly.

References

[1] L.J. Sonter, D.J. Barrett, C.J. Moran, B.S. Soares-Filho, Carbon emissions due to deforestation for the production of charcoal used in Brazil’s steel industry, Nature Climate Change 5(4) (2015) 359-363.

[2] W. Chen, Y. Xiang, M. Ding, A bottom-up analysis of China’s iron and steel industrial energy consumption and CO 2 emissions, Applied Energy 136(C) (2014) 1174-1183.

[3] P. Sheehan, E. Cheng, A. English, F. Sun, China's response to the air pollution shock, Nature Climate Change 4(5) (2014) 306-309.

[4] Y. Yamamoto, M.P. Brady, Z.P. Lu, P.J. Maziasz, C.T. Liu, B.A. Pint, K.L. More, H.M. Meyer, E.A. Payzant, Creep-resistant, Al2O3-forming austenitic stainless steels, Science 316(5823) (2007) 433-436.

[5] R. Haynes, Development of sintered low alloy steels, Powder Metall. 32(2) (1989) 140-146.

[6] L.S. Kremnev, From high-speed tungsten steel to high-temperature molybdenum steel: A century of high-speed steel, Steel in Translation 39(12) (2009) 1111-1118.

[7] K. Stiller, L.E. Svensson, P.R. Howell, W. Rong, H.O. Andren, G.L. Dunlop, High resolution

microanalytical study of precipitation in a powder metallurgical high speed steel, Acta Metall. 32(9) (1984) 1457-1467.

[8] W. Rong, H.O. Andrén, H. Wisell, G.L. Dunlop, The role of alloy composition in the precipitation behaviour of high speed steels, Acta Metall. Mater. 40(7) (1992) 1727-1738.

[9] F. Pan, P. Ding, S. Zhou, M. Kang, D.V. Edmonds, Effects of silicon additions on the mechanical properties and microstructure of high speed steels, Acta Mater. 45(11) (1997) 4703-4712.

[10] A. Lawley, Atomization of Specialty Alloy Powders, JOM 33(1) (1981) 13-18.

[11] H.T. Cao, X.P. Dong, Z. Pan, X.W. Wu, Q.W. Huang, Y.T. Pei, Surface alloying of high-vanadium high-speed steel on ductile iron using plasma transferred arc technique: Microstructure and wear properties, Mater. Des. 100 (2016) 223-234.

[12] F.A. Kirk, Problems in High-Speed Steel Manufacture and Use: A Challenge for Economic Powder Metallurgy Processing, Powder Metall. 24(2) (1981) 70-74(5).

[13] E.-S. Lee, W.-J. Park, K.-H. Baik, S. Ahn, Different carbide types and their effect on bend properties of a spray-formed high speed steel, Acta Metall. 30(8) (1998) 1133-1138.

[14] B. Šuštaršič, L. Kosec, M. Jenko, V. Leskovšek, Vacuum sintering of water-atomised HSS powders with MoS2 additions, Vacuum 61 (2001) 471–477.

[15] G. Herranz, A. Romero, V. de Castro, G.P. Rodríguez, Processing of AISI M2 high speed steel reinforced with vanadium carbide by solar sintering, Mater. Des. 54 (2014) 934-946.

[16] G.I. Parabina, O.M. Kirillova, A.F. Palamarchuk, V.T. Zubkova, Effect of oxygen and microporosity on some properties of a sintered high-speed steel, Soviet Powder Metallurgy & Metal Ceramics 19(5) (1980) 341-344.

[17] H.C.H. Carpenter, The influence of phosphorus and sulphur on the mechnical properties of steel, Nature 98 (1917) 410-411.

[18] S. Pasebani, I. Charit, Y.Q. Wu, D.P. Butt, J.I. Cole, Mechanical alloying of lanthana-bearing nanostructured ferritic steels, Acta Mater. 61(15) (2013) 5605-5617.

[19] P.E. Waudby, Rare earth additions to steel, International Materials Reviews volume 23(1) (1978) 74-98(25).

[20] C. Dominguez, Steam oxidation of boron carbide–stainless steel liquid mixtures, Journal of Nuclear Materials 427(1-3) (2012) 140-151.

[21] O.S. Bobkova, T.V. Svistunova, Impact of boron on melt properties and structurization of iron and nickel-based steels and alloys, Metallurgist 52(3-4) (2008) 175-181.

[22] S.R. Keown, F.B. Pickering, Some Aspects Of The Occurrence Of Boron In Alloy Steels, Metal Science (7) (1977) 225-234.

[23] L. Karlsson, H. Nordén, Overview no. 63 Non-equilibrium grain boundary segregation of boron in austenitic stainless steel—IV. Precipitation behaviour and distribution of elements at grain boundaries, Acta Metall. 36 (1988) 35–48.

[24] J.R. Miller, The direct reduction of iron ore, Scientific American 235 (1976) 68 - 80.

[25] Y. Torres, D. Casellas, M. Anglada, L. Llanes, Fracture toughness evaluation of hardmetals: influence of testing procedure, International Journal of Refractory Metals & Hard Materials 19(19) (2001) 27-34.

[26] M. Godec, B.Š. Batič, D. Mandrino, A. Nagode, V. Leskovšek, S.D. Škapin, M. Jenko, Characterization of the carbides and the martensite phase in powder-metallurgy high-speed steel, Mater. Charact. 61(4) (2010) 452-458.

[27] M. Pellizzari, A. Fedrizzi, M. Zadra, Influence of processing parameters and particle size on the properties of hot work and high speed tool steels by Spark Plasma Sintering, Mater. Des. 32(4) (2011)

1796-1805.
[28] M.R. Ripoll, N. Ojala, C. Katsich, V. Totolin, C. Tomastik, K. Hradil, The role of niobium in improving toughness and corrosion resistance of high speed steel laser hardfacings, Mater. Des. 99 (2016) 509-520.
[29] K.T. KIM, Y.C. JEON, Densification behavior and grain growth of tool steel powder under high temperature, Acta Metall. 46(16) (1998) 5745-5754.
[30] Z.Y. Liu, N.H. Loh, K.A. Khor, S.B. Tor, Sintering activation energy of powder injection molded 316L stainless steel, Scripta Mater. 44(7) (2001) 1131-1137.
[31] P. Matteazzi, F. Wolf, Mechanomaking of high speed steel AISI M2: powder consolidation, Mater. Sci. Eng., A A248 (1998) 19-34.
[32] A. Akash, M.J. Mayo, Pore Growth during Initial-Stage Sintering, J. Am. Ceram. Soc. 82(11) (1999) 2948–2952.
[33] R.M. German, Sintering Densification, Grain Growth, and Microstructure, International Journal of Powder Metallurgy (2005).
[34] R.M. German, Sintering Theory and Practice, 1996.
[35] E. Kawasaki, J. Sanscrainte, T.J. Walsh, Kinetics of reduction of iron oxide with carbon monoxide and hydrogen, Aiche Journal 8(1) (1962) 48-52.
[36] A.F. Rousseau, J.G. Partridge, Y.M. Gözükara, S. Gulizia, D.G. McCulloch, Carbon evolution during vacuum heat treatment of High Speed Steel, Vacuum 124 (2016) 85-88.
[37] M.A. Spears, A.G. Evans, Microstructure development during final/ intermediate stage sintering—II. Grain and pore coarsening, Acta Metall. 30(7) (1982) 1281–1289.
[38] C.H. Hsueh, A.G. Evans, R.L. Coble, Microstructure development during final/intermediate stage sintering—I. Pore/grain boundary separation, Acta Metall. 30(7) (1982) 1269–1279.
[39] R.L. Coble, Reactive sintering, Sinter-Theory and Practice: Proc. 5th Int. Round Table Conf. on Sintering, Beograd, 1981.
[40] R.L. Coble, Sintering Crystalline Solids. I. Intermediate and Final State Diffusion Models, Journal of Applied Physics 32(5) (1961) 55-67.
[41] S.J.L. Kang, Y.I. Jung, Sintering Kinetics at Final Stage Sintering: Model Calculation and Map Construction, Acta Mater. 52(15) (2004) 4573-4578.
[42] G. Neumann, C. Tuijn, Chapter 8 - Self-Diffusion and Impurity Diffusion in Group VIII Metals, Pergamon Materials (08) (2008) 259–316.
[43] H.M. Lee, S.M. Allen, Coarsening resistance of M2C carbides in secondary hardening steels: Part III. Comparison of theory and experiment, Metallurgical Transactions A 22(12) (1991) 2877-2888.
[44] J. Lentz, A. Röttger, W. Theisen, Solidification and phase formation of alloys in the hypoeutectic region of the Fe–C–B system, Acta Mater. 99 (2015) 119-129.
[45] L. Karlsson, H. Nordén, H. Odelius, Overview no. 63 Non-equilibrium grain boundary segregation of boron in austenitic stainless steel—I. Large scale segregation behaviour, Acta Metall. 36(1) (1988) 1–12.
[46] B. Hwang, D.-W. Suh, S.-J. Kim, Austenitizing temperature and hardenability of low-carbon boron steels, Scripta Mater. 64 (2011) 1118-1120.
[47] D. Casellas, J. Caro, S. Molas, J.M. Prado, I. Valls, Fracture toughness of carbides in tool steels evaluated by nanoindentation, Acta Mater. 55(13) (2007) 4277-4286.

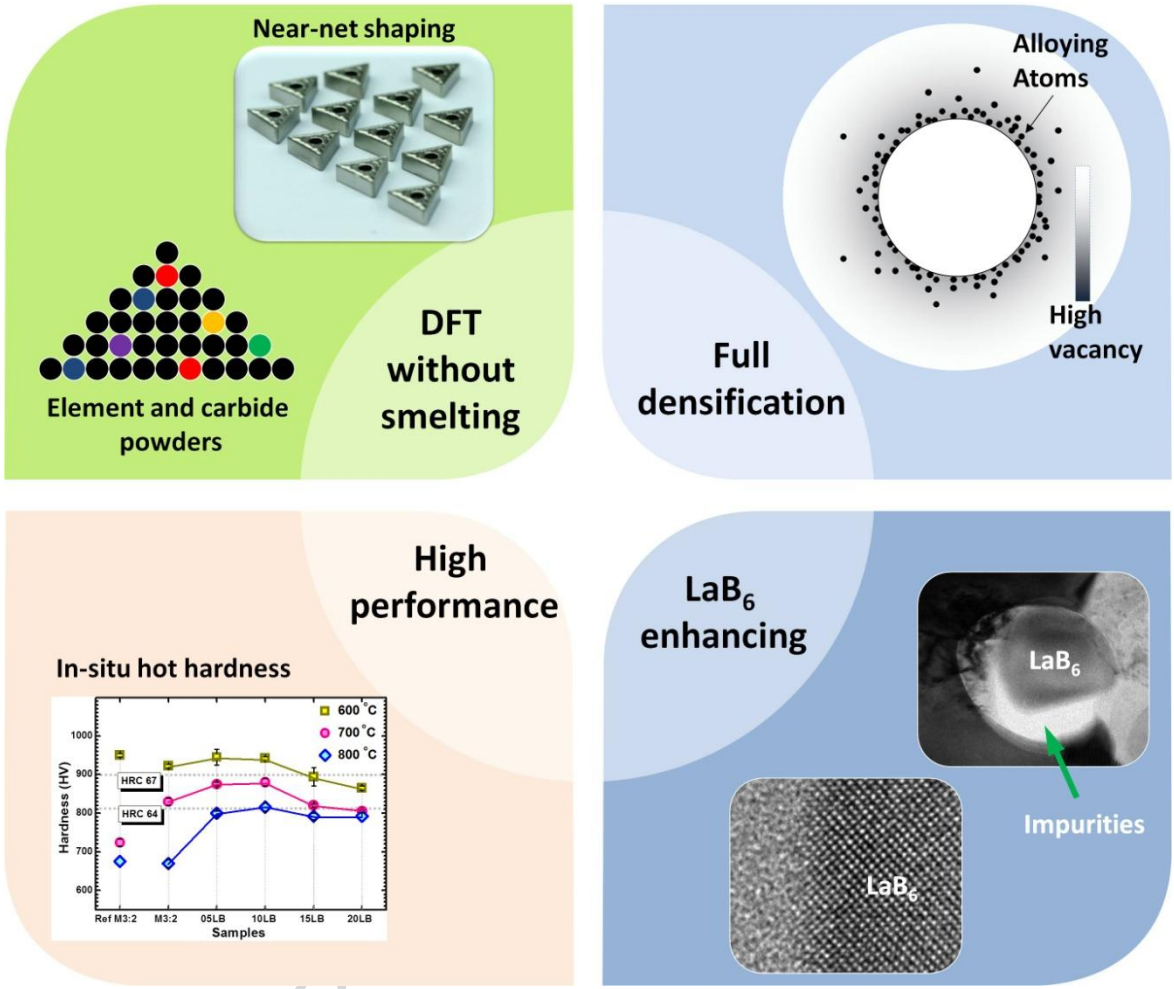

Graphical Abstract

Highlights

1. A convenient method for manufacturing near-net-shaped powder metallurgy high speed steels using mixed powders and vacuum sintering was proposed.
2. Near full densification (**>** 99.4%) was obtained via enhanced activated sintering and reactive sintering involving element segregation.
3. The strength, toughness, and hot hardness of reference steels were obviously modified by LaB_6 additions.
4. The purifying effect of LaB_6 was proved by a core-shell structure with LaB_6 as core and impurities as shell.